Ultra-Stretchable Microfluidic Devices for Optimizing Particle Manipulation in Viscoelastic Fluids

Xiaoyue Kang, Jingtao Ma, Haotian Cha, Helena H.W.B. Hansen, Xiangxun Chen, Hang T. Ta, Fangbao Tian, Nam-Trung Nguyen, Alexander Klimenko, Jun Zhang,* and Dan Yuan*
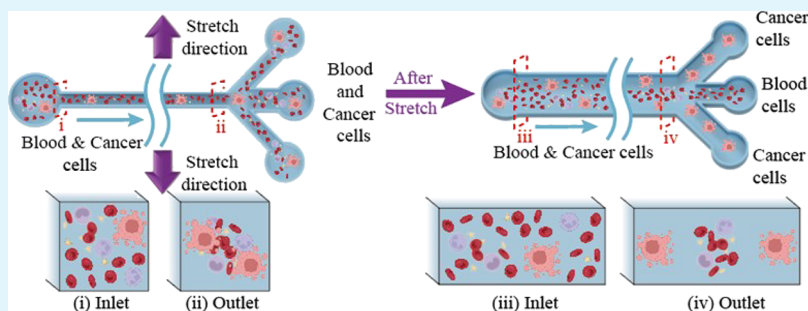
Read Online

ACCESS | 📊 Metrics & More | 📖 Article Recommendations | 🆂🅸 Supporting Information

ABSTRACT: Viscoelastic microfluidics leverages the unique properties of non-Newtonian fluids to manipulate and separate micro- or submicron particles. Channel geometry and dimension are crucial for device performance. Traditional rigid microfluidic devices require numerous iterations of fabrication and testing to optimize these parameters, which is time-consuming and costly. In this work, we developed a flexible microfluidic device using ultra-stretchable and biocompatible Flexdym material to overcome this issue. Our device allows for simultaneous modification of channel dimensions by external stretching. We fabricated a stretchable device with an initial square microchannel (30 μm × 30 μm), and the channel aspect ratio can be adjusted from 1 to 5 by external stretching. Next, the effects of aspect ratio, particle size, flow rate, and poly(ethylene oxide) (PEO) concentration that make the fluid viscoelastic on particle migration were investigated. Finally, we demonstrated the feasibility of our approach by testing channels with an aspect ratio of 3 for the separation of both particles and cells.

KEYWORDS: viscoelastic fluids, particle separation, viscoelastic microfluidics, stretchable microfluidic device, cell separation, cancer cell separation

1. INTRODUCTION

Cell separation is a fundamental technique in scientific research, with applications spanning medicine,[1] food safety,[2] and biotechnology.[3] Traditional methods such as centrifugation, filtration, flow cytometry, and fluorescence-activated cell sorting are commonly used but often face limitations such as lengthy processing times, bulky equipment, and high costs.[4−7]

Microfluidic technology offers a promising alternative for cell separation, characterized by low cost, minimal sample consumption, high detection sensitivity, and fast processing. These techniques are divided into active methods, which use external physical fields (e.g., acoustophoresis,[8,9] optical,[10,11] dielectrophoresis,[12,13] and magnetophoresis[14,15]), and passive methods, which rely on channel structures to induce hydrodynamic phenomena (e.g., pinched flow fractionation (PFF),[16,17] deterministic lateral displacement (DLD),[18,19] hydrodynamic filtration,[20,21] inertial microfluidics,[22,23] and viscoelastic microfluidics[24,25]).

Viscoelastic microfluidics, in particular, leverages the unique properties of non-Newtonian fluids to manipulate micro- and nanoparticles within simple channels without external force fields.[26−28] This method is gaining attention for its high sensitivity and simplicity, making viscoelastic microfluidics a promising technology for various applications. Notably, the geometry and size of the channel are critical factors for the effective manipulation and separation of particles.

However, predicting particle migration behavior in channels of various geometry and dimensions remains a significant challenge for both numerical modeling and experiments. Existing numerical simulation methods struggle to provide quick and accurate predictions due to complex nonlinear properties of viscoelastic fluids, the intricate interactions between particles and fluid flow, and the expertise and
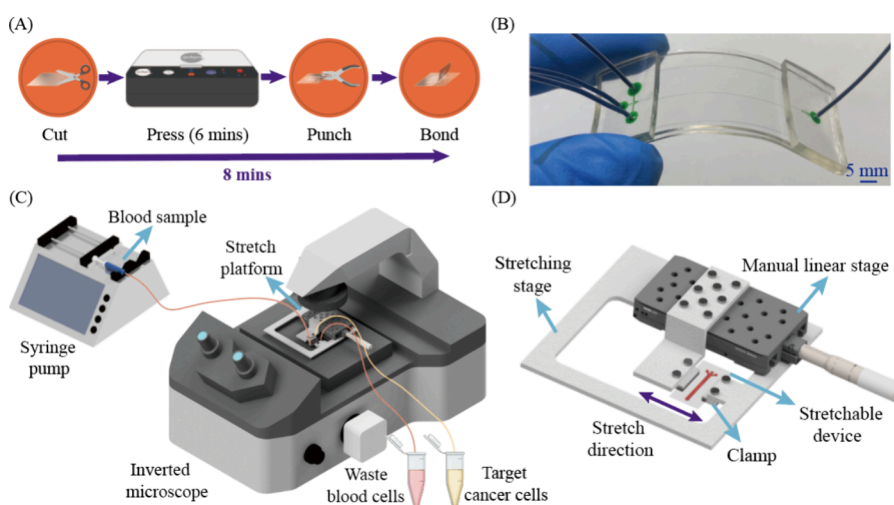
Figure 1. Device fabrication and experiment setup. (A) Fabrication process for the Flexdym flexible device. (B) Photo of the fabricated device. (C) Schematics of the experimental setup. (D) Custom-made mechanical stretching device.

computational resources required.[29] Moreover, experimental testing demands time-consuming and costly iterative device design and fabrication because traditional microfluidic devices made of thick polydimethylsiloxane (PDMS),[30,31] 3D-printed photosensitive resins,[32,33] and poly(methyl methacrylate) (PMMA)[34] are rigid, and the channel dimensions cannot be altered once fabricated.

Recently, flexible and stretchable microfluidics emerged by constructing devices using flexible materials or films, and real-time dynamic adjustment of channel size can be obtained.[35,36] Several researchers have demonstrated stretchable microfluidic devices fabricated using various flexible materials. Commonly used PDMS becomes more deformable when the PDMS thickness decreases.[35,37,38] Our previous work developed a flexible microfluidic technology using thin PDMS films,[36,39] but the limited strain range (<165%) of PDMS restricts a wider range adjustment of channel dimensions.[40] Hybrid silicone rubber offers large-scale stretching but reduced transparency.[41] Ecoflex is a soft and transparent silicone elastomer that can withstand 900% strain.[42] However, it is not suitable for soft lithography, restricting its use only for microchannels with rectangular cross sections and small dimensions.

In this work, we develop a novel flexible microfluidic device using Flexdym thin film materials. Flexdym, a transparent and strong thermoplastic, enables the fabrication of ultra-stretchable microfluidic devices with small-scale structures and reversible plasma bonding. By stretching the flexible microfluidic device to achieve a large range of channel aspect ratios, we study the influence of channel aspect ratio, flow rate, poly(ethylene oxide) (PEO) concentration, and particle size on particle viscoelastic migration. We choose an optimal channel aspect ratio based on the screening results and apply the device for the separation of binary particle mixture and isolation of spiked cancer cells from diluted whole blood. This flexible microfluidic platform provides a fast, cost-effective, and efficient way to optimize cell separations.

2. THEORY

2.1. Inertial Lift Force. Inertial migration is a phenomenon in which particles reach equilibrium positions within the channel cross section after a certain distance under the inertial

flow regime of Reynolds number (Re) on the order of 1 to 100.[43,44] In this work, as the flow rate increases, the inertial forces of the fluid become significant, causing particles to migrate under the influence of inertial lift.[45] The inertial lift primarily consists of two components: the wall lift force F_{LW}, resulting from the interaction between the fluid and the channel wall, and the shear gradient lift force F_{LS}, due to the uneven distribution of fluid velocity.[46] These forces act to repel particles toward the channel center and guide them along the channel wall, respectively. When the microchannel dimensions are substantially larger than the particle size, the net inertial lift force F_L is[47]

$$F_L = \frac{\rho U_m^2 a^4}{D_h^2} f_L(Re, z) \tag{1}$$

where ρ is the fluid density, U_m is the maximum flow velocity, a is the particle diameter, D_h is the hydraulic diameter of the channel, $f_L(Re,z)$ is the lift coefficient, related to the Re and the particle position in the channel.

2.2. Drag Force. The velocity difference between the particle and the fluid generates a drag force acting on the particle. Based on Stokes law, this drag force can be expressed as[48]

$$F_D = 6\pi\mu R_p(U_f - U_p) \tag{2}$$

where μ, R_p, U_f, and U_p are the dynamic viscosity particle radius, fluid, and particle velocities, respectively.

2.3. Elastic Force. Viscoelastic fluids exhibit unique rheological properties. The ratio of elastic to viscous forces, defined as the Weissenberg number (Wi) or Deborah number (De), describes the fluid's elasticity.[49]

$$Wi = \frac{\lambda}{t_f} = \lambda\dot{\gamma} = \lambda\frac{2U_m}{D_h} \tag{3}$$

where λ is the fluid relaxation time, t_f is the characteristic time of fluid flow, and $\dot{\gamma}$ is the average (characteristic) shear rate and can be calculated by ($2U_m/D_h$).

The elasticity number (El) is a dimensionless quantity to compare the relative strengths of inertia and elastic effects.[50]
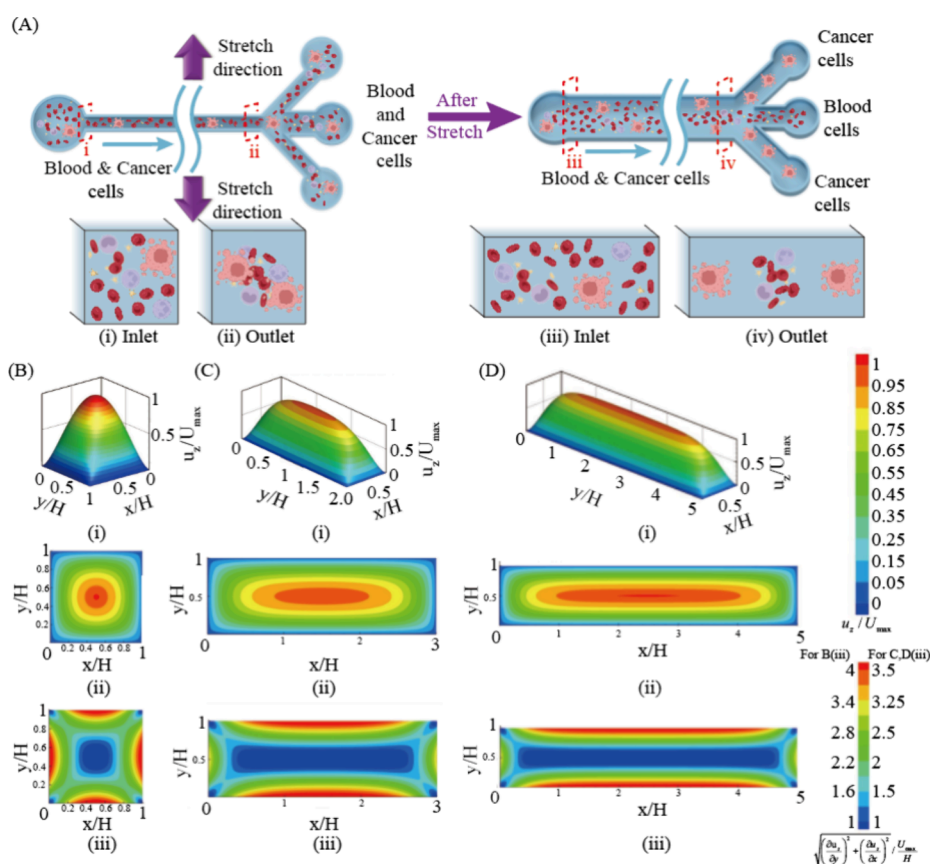
Figure 2. Schematic of cell migration. (A) AR = 1 and AR = 3 channel, (i) AR = 1 channel inlet cross section, (ii) AR = 1 channel outlet cross section, (iii) AR = 3 channel inlet cross section, (iv) AR = 3 channel outlet cross section. (B−D) Simulation results of flow fields for channel aspect ratios (ARs) of 1, 3, and 5, respectively. (i) 3D flow field, (ii) flow velocity, and (iii) shear rate.

$$El = \frac{Wi}{Re} = \frac{2\lambda\mu}{\rho_f D_h^2} \tag{4}$$

The distribution of normal stress of viscoelastic flow is nonuniform, resulting in elastic forces (F_E) on particles.[51] The first normal stress difference ($N_1 = \tau_{xx} - \tau_{yy}$) significantly contributes to the generation of elastic forces in diluted viscoelastic solutions. τ_{xx} and τ_{yy} denote the normal stresses directed toward the flow and the velocity gradient.[52,53]

$$N_1 = -2\eta_p\lambda\dot{\gamma}^2 \tag{5}$$

$$\nabla N_1 = \nabla\tau_{xx} - \nabla\tau_{yy} = -2\eta_p\lambda\nabla\dot{\gamma}^2 \tag{6}$$

$$F_E = C_{eL}a^3\nabla N_1 \tag{7}$$

Here, η_p is the polymeric contribution to the solution viscosity, and C_{eL} is the nondimensional elastic lift coefficient.

3. MATERIALS AND METHODS

3.1. Device Design and Fabrication. In this work, the flexible microfluidic device was fabricated from Flexdym (Eden Tech Microfluidics, Paris, France), a new soft thermoplastic elastomer material. This material has similar transparency, cost-effectiveness, and high pattern resolution as PDMS. However, Flexdym has much higher flexibility and stretchability, with maximum strain of a single piece as high as 720%.[54−56] First, the standard photolithography technique was used to fabricate the silicon master mold. Second, a Flexdym sheet (thickness of 250 μm) was sandwiched between the silicon wafer master mold and a blank silicon wafer. Third, this sandwich was compressed for 360 s at a temperature of 165 °C using

the vacuum hot-pressing machine SuBlym100 (Eden Tech Microfluidics, Paris, France). Peeling the Flexdym sheet off the silicon module, microchannel features were replicated on the surface of the Flexdym sheet (Figure 1A).[57,58] Subsequently, the inlet and outlet holes were punched before the sheet was bonded with another blank Flexdym substrate using plasma cleaning. Two thick Flexdym slabs were bonded at the inlet and outlet regions for the firm collection of inlet and outlet tubing (Figure 1B). The width and height of the straight channel are both 30 μm. The length of the channel is 3 cm. The width and aspect ratio (AR = channel width/channel height) of the straight channel were changed by stretching. To precisely predict the microchannel width and height variations under stretching, we measured the Poisson's ratio of the Flexdym bonded device to be approximately 2.62 (details in Supplementary S1). The exceptional stretchability of Flexdym materials after plasma bonding allows elongation of up to 1050.8% from our tests (Supplementary S2).

3.2. Viscoelastic Fluid Preparation. PEO (2,000,000 Da, Sigma-Aldrich) was dissolved in deionized (DI) water to obtain viscoelastic solutions with concentrations of 500, 1000, and 2000 ppm, respectively. Tween 20 (Sigma-Aldrich, product no. P9416) with a volume ratio of 0.1% was added to prevent particle aggregation.

For cell experiments, PEO (2,000,000 Da, Sigma-Aldrich) was dissolved in phosphate-buffered saline (PBS) to obtain a PEO concentration of 4000 ppm. Then, 4000 ppm PEO solution and PBS were used to dilute the whole blood to achieve the diluted blood sample (×1/5) with a final PEO solution concentration of 2,000 ppm.

3.3. Particle Preparation. Three sets of spherical polystyrene microbeads (Thermo Fisher Scientific, product nos. G0500 and G1000; Phosphorex, product no. 1015KR) of 4.8, 9.9, and 15 μm diameters were suspended into 500, 1000, and 2000 ppm PEO solution, respectively. The concentration of the polystyrene particles
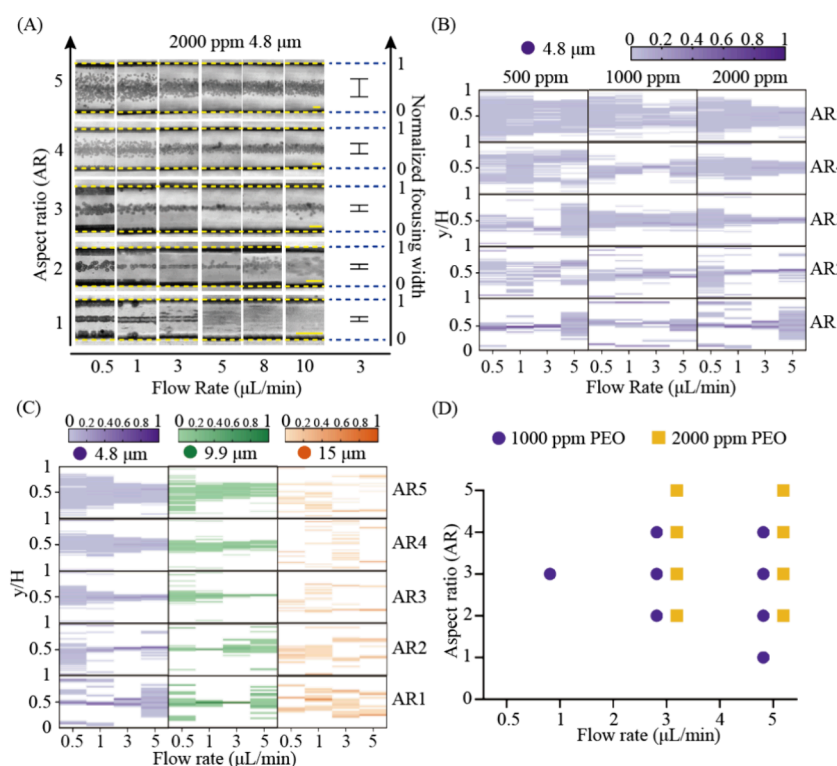
Figure 3. (A) Channel outlet experimental distribution of 4.8 μm particles in 2000 ppm PEO solution with 0.5 to 10 μL/min flow rates, from the aspect ratio of 1 to 5. The scale bar length is 20 μm. (B) Dimensionless and normalized particle distributions of 4.8 μm particles in different concentration PEO solutions along the channel width at the channel outlet. The flow rate is from 0.5 to 5 μL/min for the different aspect ratio channels. The flow rate is from 0.5 to 5 μL/min for the different aspect ratio channels. (C) Dimensionless and normalized particle distributions of 4.8, 9.9, and 15 μm particles in 2000 ppm PEO solution along the channel width at the channel outlet. The flow rate is from 0.5 to 5 μL/min for the different aspect ratio channels. (D) Separation region summary. Purple dots represent particles of 4.8 and 9.9 μm in 1000 ppm PEO solution, and yellow dots represent particles of 4.8/9.9 and 15 μm in 2000 ppm PEO solution.

was prepared with the concentrations of 7.2×10^5, 8.99×10^4, and 2.66×10^4 counts per mL, respectively.

3.4. Preparation of Blood and Cancer Cells. The blood sample was obtained from a healthy volunteer with approved Human Research Ethics (protocol number 2021/598, Griffith University). All experiments were performed in compliance with applicable laws and institutional guidelines. Human Breast Cancer cells (MDA-MB-231) were obtained from the American Type Tissue Culture Collection (ATCC, Manassas, VA, USA). The cell culture reagents were obtained from Thermo Fisher Scientific (Waltham, Massachusetts, USA). Cells were cultured in T75 flasks using Dulbecco's modified Eagle's medium (DMEM) with low glucose, supplemented with 10% heat-inactivated fetal bovine serum (FBS) and 1% antibiotics, in a humidified environment at 37 °C and 5% CO_2. Cells were subsequently incubated with 100 ng/mL dihexyloxacarbocyanine iodide (DiOC6) overnight under the same incubation conditions. The incubated cells were detached using TrypLE Express Enzyme for 5 min. Following this, 4 mL of DMEM was added to the flask. The DiOC6-stained cells were then centrifuged at 500g for 5 min at room temperature. The resulting cell pellets were resuspended in 1 mL of DMEM, and the stained cells were observed under the microscope to confirm successful fluorescence staining. To assess the device separation performance, cancer cells were spiked into diluted whole blood samples (1/5) at a ratio of 0.02%; after that, the final diluted ratio was 1/15, where the cancer cell concentration was approximately 1.15×10^6 counts/mL.

3.5. Experimental Setup. A mechanical stretching device, which consists of a manual linear stage (Thorlabs, XR50C) and PMMA frames, was placed under an inverted microscope (OLYMPUS, IX73P1F) (Figure 1C,D). The sample suspension was infused into the microfluidic device using a 1 mL disposable syringe (BD, 302100), and a syringe pump (SHENCHEN ISPLab002) was used to

control the flow rate of the sample injection. A high-speed camera system (Phantom VEO-L) was mounted to the microscope to record particle positions and fluorescence trajectories in the microchannel. The open-source software ImageJ (National Institutes of Health) was employed to process and analyze videos and images. The transverse distributions of particles were normalized and illustrated in a color-coded map.[59]

4. RESULTS AND DISCUSSION

4.1. Working Mechanism. Our working mechanism relies on channel aspect ratio-dependent particle migration behavior in viscoelastic fluids. Microchannels with various channel aspect ratios can be obtained through lateral stretching on a single flexible device. The channel aspect ratios can be screened for particles and cells of various sizes so that an optimal aspect ratio can be determined for the efficient separation of target particles or cells (Figure 2A).

We simulated the flow field of viscoelastic fluids in microchannels with ARs of 1, 3, and 5, as shown in Figure 2B−D (more details in Supplementary S3). It can be observed that as the channel width is increased by stretching, the velocity profile flattens. The maximum flow velocity area shifts from a central point to a broader oval region (Figure 2B−D, (i) and (ii)). From Figure 2B−D(iii), the maximum average shear rate was decreased with increasing AR. The minimum average shear rate area also alters accordingly, spanning a larger central region along the stretching direction. The enlarged low average shear rate region leads to a reduction of the shear rate gradient within that area. This further inhibits the generation
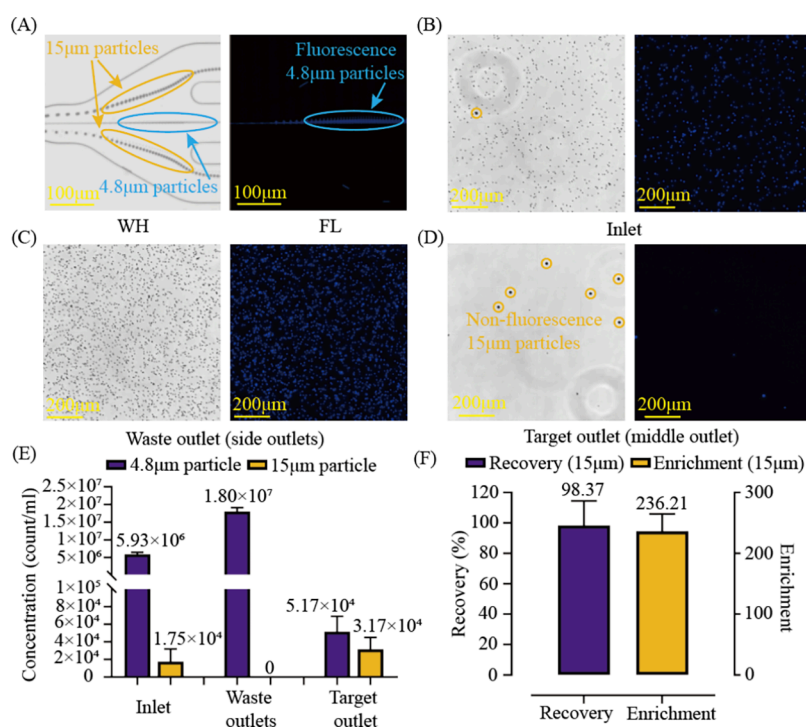
Figure 4. Separation performance of 4.8 and 15 μm particles in a microchannel with AR3. (A) Particle migration trajectory microscopic images with bright-field (WH) and fluorescence field (FL). (B−D) Microscopic images of particle samples at the inlet and outlets under a hemocytometer, only the 4.8 μm particles with blue fluorescence. (E) Concentrations of 4.8 and 15 μm particles before and after processing through the device. (F) Recovery (or separation efficiency is the ratio of collected target particle number to input target particle number) and enrichment ratio (purity of target outlet to purity of inlet) of 15 μm particles after processing. The particle number and the collected particles were measured three times and then averaged.

of strong normal stress differences on particles across those areas. Therefore, particles tend to be defocused and dispersed in those low shear rate gradient regions.

Additionally, the particle equilibrium position is determined by the particle blockage ratio, and the effect of normal stresses is strengthened by the effect of the blockage ratio.[60−62] When the particle size exceeds a threshold, they tend to have bilateral focusing along the wider direction. As particles are displaced from the centerline, the fluid tends to flow through the larger gap between the particles and the wall. Therefore, the particles will be driven toward the sidewalls under enhanced compressive normal stress near the center,[60−62] whereas the particles with a blockage ratio below the threshold will tend to migrate to the channel center area, regardless of the initial positions. Based on this effect of blockage ratio, particles with different sizes can be induced to different equilibrium positions, achieving separation. The separation performance is expected to be enhanced in channels with optimal AR by stretching, as illustrated in Figure 2A(i)−(iv).

4.2. Effects of Channel Aspect Ratio by Lateral Stretching. To investigate the effect of aspect ratio, we tested 4.8 μm particle migration behavior in 2000 ppm PEO solutions during device lateral stretching (Figure 3A). The investigated aspect ratio ranged from 1 to 5, and the flow rates were from 0.5 to 10 μL/min. The corresponding Reynolds number Re, Wi, and El for each flow rate and aspect ratio are demonstrated in Supplementary S4.

The original channel before stretching has a square cross section (AR = 1). At a low flow rate with $Q = 0.5$ μL/min ($Re = 0.185$, $Wi = 12.037$, El = 65.196), the fluid viscoelasticity dominates particle migration. Particles migrated to low shear

rate regions, corresponding to the channel center and four corners. As the flow rate increased to $Q = 3$ μL/min ($Re = 1.108$, $Wi = 72.222$, El = 65.196), inertial effects became more obvious, leading to particle elasto-inertial single line focusing at the channel center. Then, flow rate increased further to $Q = 5$ μL/min ($Re = 1.864$, $Wi = 120.370$, El = 65.196), and inertial effects started to dominate, presented as particles started to be dispersed.

When particles flow in a channel with a different AR, a similar particle migration pattern can still be observed. Particles undergo from a viscoelasticity dominant focusing to an elasto-inertial focusing and defocus after that. Figure 3 shows that as the aspect ratio increases, the effective flow rate range for particle elasto-inertial focusing increases. This can be evidenced by the single-line focusing observed only at $Q = 3$ μL/min for AR = 1, at $Q = 3−5$ μL/min for AR = 2, and at $Q = 3−10$ μL/min for AR > 3. However, the particle elasto-inertial focusing width was enlarged and presented as particles dispersed in a larger center area. This is because the enlarged low shear rate gradient region due to stretching inhibits the generation of strong normal stress differences on particles across those areas. The normalized particle focusing width was increased as the aspect ratio increased from 1 to 5 at a flow rate of $Q = 3$ μL/min (Figure 3A).

4.3. Effects of Different Polymer Concentrations. We also investigated the effects of PEO concentrations on particle equilibrium positions within the stretchable microfluidic device. In the 500 ppm PEO solution (Figure 3B, left column), the weak viscoelastic effect fails to generate sufficient elastic force to pull particles to the center equilibrium position, leading to random particle distribution throughout the
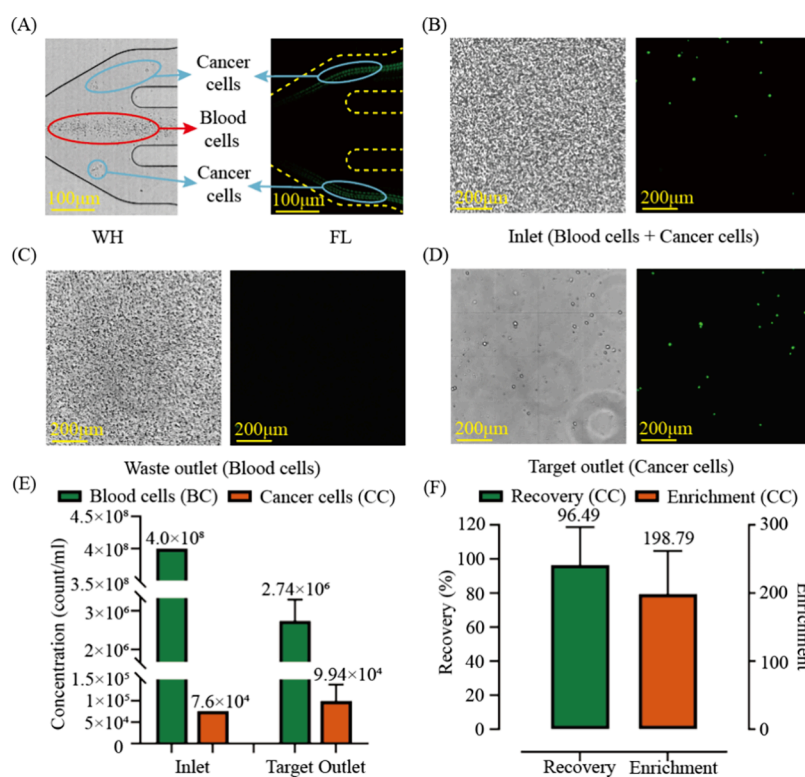
Figure 5. (A−D) Microscopic images of blood samples at the inlet and outlets under a hemocytometer. Only the cancer cells are stained with green fluorescence. (B) High-speed image shows the distribution of blood and cancer cells at the trifurcation area of the channel. (E) Concentration of the blood and cancer cells before and after processing through the device. (F) Recovery (or separation efficiency) and enrichment of cancer cells after processing. All collected cells were measured three times and then averaged.

channel. This distribution remains largely unaffected by increased flow rates. At 1000 ppm (Figure 3B, middle column), the viscoelasticity of the fluid starts to become more effective. At lower flow rates, where elastic lift force dominates and inertial effects are negligible, particles migrate to positions with the smallest shear rate, corresponding to the channel center and four corners. As flow rates increase, competing inertial and elastic forces cause particles near the walls to be pushed toward the channel center, resulting in elasto-inertial single-line focusing at the center. The fluid viscoelasticity increases further with 2000 ppm PEO concentration, demonstrated by an improved focusing performance under elasto-inertial focusing regime (Figure 3B, right column). The results revealed that a moderate increase in PEO concentration can enhance the focusing performance.

4.4. Effects of Particle Size. Apart from the channel aspect ratio and polymer concentrations, particle size can also significantly affect particle migration in viscoelastic fluids. Differently sized particle migration was demonstrated in 2000 ppm PEO solutions (Figure 3C). We calculated the blockage ratio (the ratio of particle diameter to channel hydraulic diameter a/D_h). For 4.8 μm particles, the ratio increases from 0.128 to 0.160, leading to single-beam focusing, with a better-focusing performance as the flow rate increases. For 9.9 μm particles, the ratio ranges from 0.264 to 0.330, resulting in central focusing in 2000 ppm PEO solutions. However, 9.9 μm particles also presented bilateral focusing and strong dependence on the solution PEO concentration (Supplementary S5A).

For 15 μm particles, the ratio rises from 0.400 to 0.500, leading to bilateral focusing and increasing transverse distance with higher aspect ratios. It has been reported that the bilateral migration is due to the effect of the blockage ratio.[60−62] As the particle sizes exceed a threshold, when particles are displaced from the centerline, the fluid tends to flow through the larger gap between the particles and the wall. Therefore, the particles will be driven toward the sidewalls under enhanced compressive normal stress near the center. A blockage ratio of 0.5 or higher would significantly inhibit particle migration and cause strong particle interactions (Supplementary S5B−D).

4.5. Particle Separation. Test results from the flexible device revealed that a channel with many conditions can achieve particle separation, as shown in Figure 3D, and a channel with an AR of 3 achieved the highest separation possibility. Thus, we selected AR = 3 dimensions as ideal for size-based particle/cell separation. For portability, accuracy, and simplicity, we fabricated a rigid PDMS chip with these dimensions. This selection aimed to evaluate the practicability of the flexible microfluidic device for rapid device optimization for particle separation.

As anticipated by the preceding stretching experiment, at a flow rate of 3 μL/min, a distinct particle separation was observed when the channel was infused with a particle mixture with 2000 ppm PEO solution. Larger 15 μm particle equilibrium at the channel two sides and smaller 4.8 μm particles were focused on the channel center (Figure 4A and Video S1). The separation was confirmed by the bright-field and fluorescence images of particle samples at the inlet and outlet (Figure 4B−D). The nonfluorescent 15 μm particles

were indicated by yellow circles, while the blue dots represent the fluorescent 4.8 μm particles. We observed that 4.8 μm particles were almost eliminated, while the target 15 μm particles were concentrated in the targeted outlet (Figure 4D).

We quantitatively analyzed the separation performance by measuring the concentration of particles at the inlet and outlets. A hemocytometer was used to count the particle number, and the collected particles were measured three times and then averaged. The concentration of 4.8 μm particles is increased by one order of magnitude in the waste outlet from 5.93×10^6 to 1.8×10^7 counts/mL, while it was reduced by two orders of magnitude in the target outlet to 5.17×10^4 counts/mL (Figure 4E). Negligible 15 μm particles were captured in the waste outlet, and the recovery efficiency for 15 μm particles reached 98.37% with a significant enrichment ratio of 236.21 (Figure 4F).

4.6. Cancer Cell Separation. Based on our device optimization study for particle separation, we further applied the optimal viscoelastic microfluidic device for cell separation. Given that the sizes of the relevant particles closely approximate those of red blood cells and cancer cells, we utilized this device to isolate cancer cells from diluted human whole blood, thereby verifying its strong potential in disease diagnosis. We spiked fluorescently labeled human breast cancer cells (MDA-MB-231) into the diluted whole blood sample (5×) at a concentration of 0.02%. The spiked sample was introduced into the device at a flow rate of 3 μL/min.

Utilizing bright-field and fluorescent imaging, they demonstrate that cancer cells are displaced from the central axis of the channel, migrate toward the regions near the sidewalls, and are subsequently concentrated at the two outer outlets (Figure 5A and Video S2). In comparison, blood cells are focused on the central outlet. The samples were then collected separately from the outlets. The bright-field and fluorescence images of the initial samples and different outlets are in Figure 5B−D. The high density of blood cells at the inlet made it challenging to visually detect cancer cells, necessitating reliable fluorescence identification. However, at the outlet, blood cells are massively removed, and the cancer cells were significantly enriched to be visually observable.

The quantitative analysis presented in Figure 5E shows that the concentration of cancer cells increased from 7.6×10^4 to 9.94×10^4 counts/mL in the targeted outlets, while the concentration of blood cells decreased by two orders of magnitude, from 4×10^8 to 2.74×10^6 counts/mL. The recovery rate of cancer cells reached 96.49%, with an enrichment ratio of 198.79 (Figure 5F). All collected cells were measured three times and then averaged.

5. CONCLUSIONS

This work presents a novel approach to investigate the elasto-inertial separation behavior of particles, utilizing stretchable elasto-inertial microfluidic systems to achieve adjustable channel sizes and rapid optimization of particle and cell separation. We conducted a systematic experimental study to examine the effects of flow rate, polymer concentration, particle size, and channel aspect ratio on elasto-inertial particle migration. Our findings demonstrate that lateral stretching of the microchannel alters the channel's aspect ratio to facilitate the rapid and controllable separation of target particle/cell sizes. Leveraging the exceptional stretchability of Flexdym materials, the plasma-bonded microchannels can extend more than 1000%. We believe that the ultra-stretchable microfluidic

platform, made from highly flexible, biocompatible materials, holds significant potential for efficient optimization of cell separation in disease diagnosis.

■ ASSOCIATED CONTENT

ⓈI Supporting Information

The Supporting Information is available free of charge at https://pubs.acs.org/doi/10.1021/acsami.4c15893.

> (Supplement S1) Flexdym Poisson ratio calculation and the aspect ratio corresponding channel dimensions after stretching; (Supplement S2) plasma-bonded Flexdym chip tensile strength test; (Supplement S3) simulation method of the flow field and shear rate of viscoelastic fluids in microchannels; (Supplement S4) experiment flow rate corresponding to Reynolds number (Re), Weissenberg number (Wi), and elasticity number (El) calculation; and (Supplement S5) 9.9 and 15 μm particles normalized focusing pattern (PDF)

> (Supplement V1) Particle separation video (MP4)

> (Supplement V2) Cancer cell separation video (MP4)

■ AUTHOR INFORMATION

Corresponding Authors

Jun Zhang − *Queensland Micro and Nanotechnology Centre, Griffith University, Brisbane, Queensland 4111, Australia; School of Engineering and Built Environment, Griffith University, Nathan, Queensland 4111, Australia;* ◎ orcid.org/0000-0003-1113-6264; Email: jun.zhang@griffith.edu.au

Dan Yuan − *School of Mechanical and Mining Engineering, University of Queensland, Brisbane, Queensland 4067, Australia;* ◎ orcid.org/0000-0002-5472-232X; Email: d.yuan@uq.edu.au

Authors

Xiaoyue Kang − *School of Mechanical and Mining Engineering, University of Queensland, Brisbane, Queensland 4067, Australia*

Jingtao Ma − *School of Engineering and Information Technology, University of New South Wales, Canberra, ACT 2600, Australia*

Haotian Cha − *Queensland Micro and Nanotechnology Centre, Griffith University, Brisbane, Queensland 4111, Australia*

Helena H.W.B. Hansen − *Queensland Micro and Nanotechnology Centre, Griffith University, Brisbane, Queensland 4111, Australia*

Xiangxun Chen − *Queensland Micro and Nanotechnology Centre, Griffith University, Brisbane, Queensland 4111, Australia*

Hang T. Ta − *Queensland Micro and Nanotechnology Centre, Griffith University, Brisbane, Queensland 4111, Australia; Bioscience Discipline, School of Environment and Science, Griffith University, Nathan, Queensland 4111, Australia;* ◎ orcid.org/0000-0003-1188-0472

Fangbao Tian − *School of Engineering and Information Technology, University of New South Wales, Canberra, ACT 2600, Australia*

Nam-Trung Nguyen − *Queensland Micro and Nanotechnology Centre, Griffith University, Brisbane, Queensland 4111, Australia*

Alexander Klimenko − *School of Mechanical and Mining Engineering, University of Queensland, Brisbane, Queensland 4067, Australia*

Complete contact information is available at:
https://pubs.acs.org/10.1021/acsami.4c15893

Author Contributions

D.Y., J.Z., and N.-T.N. conceived the idea and designed and supervised the project. X.K. fabricated the ultra-stretchable microfluidic devices, prepared the particle samples and blood samples, performed all the experiments, analyzed and prepared experimental data for visualization, and contributed to the original draft and Supporting Information. J.M. and F.T. developed the numerical methods for LBM, performed simulations, visualized simulation figures, and contributed to the Supporting Information. H.C. and A.K. revised the figures and contributed to the original draft and Supporting Information. H.H.W.B.H., X.C., and H.T.T. contributed to the biological cell preparation. All authors provided critical feedback and read and approved the manuscript.

Notes

The authors declare no competing financial interest.

■ REFERENCES

(1) Bayareh, M. An updated review on particle separation in passive microfluidic devices. *Chemical Engineering and Processing-Process Intensification* **2020**, *153*, No. 107984.

(2) Su, P.; Ren, C.; Fu, Y.; Guo, J.; Guo, J.; Yuan, Q. Magnetophoresis in microfluidic lab: Recent advance. *Sensors and Actuators A: Physical* **2021**, *332*, No. 113180.

(3) Tomlinson, M. J.; Tomlinson, S.; Yang, X. B.; Kirkham, J. Cell separation: Terminology and practical considerations. *J. Tissue Eng.* **2013**, *4*, No. 2041731412472690.

(4) Lianidou, E. S.; Markou, A. Circulating tumor cells in breast cancer: detection systems, molecular characterization, and future challenges. *Clinical chemistry* **2011**, *57* (9), 1242−1255.

(5) Alunni-Fabbroni, M.; Sandri, M. T. Circulating tumour cells in clinical practice: Methods of detection and possible characterization. *Methods* **2010**, *50* (4), 289−297.

(6) Shen, Z.; Wu, A.; Chen, X. Current detection technologies for circulating tumor cells. *Chem. Soc. Rev.* **2017**, *46* (8), 2038−2056.

(7) Ferreira, M. M.; Ramani, V. C.; Jeffrey, S. S. Circulating tumor cell technologies. *Molecular oncology* **2016**, *10* (3), 374−394.

(8) Wu, M.; Ozcelik, A.; Rufo, J.; Wang, Z.; Fang, R.; Huang, T. J. Acoustofluidic separation of cells and particles. *Microsyst. Nanoeng.* **2019**, *5* (1), 32.

(9) Rufo, J.; Cai, F.; Friend, J.; Wiklund, M.; Huang, T. J. Acoustofluidics for biomedical applications. *Nat. Rev. Methods Primers* **2022**, *2* (1), 30.

(10) Kotz, K.; Noble, K.; Faris, G. Optical microfluidics. *Applied physics letters* **2004**, *85* (13), 2658−2660.

(11) Myers, F. B.; Lee, L. P. Innovations in optical microfluidic technologies for point-of-care diagnostics. *Lab Chip* **2008**, *8* (12), 2015−2031.

(12) Bentor, J.; Malekanfard, A.; Raihan, M. K.; Wu, S.; Pan, X.; Song, Y.; Xuan, X. Insulator-based dielectrophoretic focusing and trapping of particles in non-Newtonian fluids. *Electrophoresis* **2021**, *42* (21−22), 2154−2161.

(13) Çetin, B.; Li, D. Dielectrophoresis in microfluidics technology. *Electrophoresis* **2011**, *32* (18), 2410−2427.

(14) Munaz, A.; Shiddiky, M. J. A.; Nguyen, N.-T. Recent advances and current challenges in magnetophoresis based micro magneto-fluidics. *Biomicrofluidics* **2018**, *12* (3), No. 031501.

(15) Zeng, L.; Chen, X.; Zhang, R.; Hu, S.; Zhang, H.; Zhang, Y.; Yang, H. High-resolution separation of nanoparticles using a negative magnetophoretic microfluidic system. *Micromachines* **2022**, *13* (3), 377.

(16) Lu, X.; Xuan, X. Continuous microfluidic particle separation via elasto-inertial pinched flow fractionation. *Analytical chemistry* **2015**, *87* (12), 6389−6396.

(17) Lu, X.; Xuan, X. Inertia-enhanced pinched flow fractionation. *Analytical chemistry* **2015**, *87* (8), 4560−4565.

(18) Dincau, B. M.; Aghilinejad, A.; Hammersley, T.; Chen, X.; Kim, J.-H. Deterministic lateral displacement (DLD) in the high Reynolds number regime: High-throughput and dynamic separation characteristics. *Microfluid. Nanofluid.* **2018**, *22*, 1−8.

(19) Xiang, N.; Wang, J.; Li, Q.; Han, Y.; Huang, D.; Ni, Z. Precise size-based cell separation via the coupling of inertial microfluidics and deterministic lateral displacement. *Analytical chemistry* **2019**, *91* (15), 10328−10334.

(20) Yamada, M.; Seki, M. Hydrodynamic filtration for on-chip particle concentration and classification utilizing microfluidics. *Lab Chip* **2005**, *5* (11), 1233−1239.

(21) Yan, S.; Zhang, J.; Yuan, D.; Li, W. Hybrid microfluidics combined with active and passive approaches for continuous cell separation. *Electrophoresis* **2017**, *38* (2), 238−249.

(22) Cha, H.; Dai, Y.; Hansen, H. H. W. B.; Ouyang, L.; Chen, X.; Kang, X.; An, H.; Ta, H. T.; Nguyen, N. T.; Zhang, J. Asymmetrical obstacles enable unilateral inertial focusing and separation in sinusoidal microchannel. *Cyborg Bionic Syst.* **2023**, *4*, No. 0036.

(23) Zhang, J.; Chintalaramulu, N.; Vadivelu, R.; An, H.; Yuan, D.; Jin, J.; Ooi, C. H.; Cock, I. E.; Li, W.; Nguyen, N.-T. Inertial microfluidic purification of floating cancer cells for drug screening and three-dimensional tumor models. *Anal. Chem.* **2020**, *92* (17), 11558−11564.

(24) Yuan, D.; Zhao, Q.; Yan, S.; Tang, S.-Y.; Alici, G.; Zhang, J.; Li, W. Recent progress of particle migration in viscoelastic fluids. *Lab Chip* **2018**, *18* (4), 551−567.

(25) Yuan, D.; Zhang, J.; Sluyter, R.; Zhao, Q.; Yan, S.; Alici, G.; Li, W. Continuous plasma extraction under viscoelastic fluid in a straight channel with asymmetrical expansion−contraction cavity arrays. *Lab Chip* **2016**, *16* (20), 3919−3928.

(26) Meng, Y.; Zhang, Y.; Bühler, M.; Wang, S.; Asghari, M.; Stürchler, A.; Mateescu, B.; Weiss, T.; Stavrakis, S.; deMello, A. J. Direct isolation of small extracellular vesicles from human blood using viscoelastic microfluidics. *Sci. Adv.* **2023**, *9* (40), No. eadi5296.

(27) Liu, P.; Liu, H.; Semenec, L.; Yuan, D.; Yan, S.; Cain, A. K.; Li, M. Length-based separation of Bacillus subtilis bacterial populations by viscoelastic microfluidics. *Microsyst. Nanoeng.* **2022**, *8* (1), 7.

(28) Tian, F.; Cai, L.; Chang, J.; Li, S.; Liu, C.; Li, T.; Sun, J. Label-free isolation of rare tumor cells from untreated whole blood by interfacial viscoelastic microfluidics. *Lab Chip* **2018**, *18* (22), 3436−3445.

(29) Li, G.; McKinley, G. H.; Ardekani, A. M. Dynamics of particle migration in channel flow of viscoelastic fluids. *J. Fluid Mech.* **2015**, *785*, 486−505.

(30) Ozcelik, A.; Ahmed, D.; Xie, Y.; Nama, N.; Qu, Z.; Nawaz, A. A.; Huang, T. J. An acoustofluidic micromixer via bubble inception and cavitation from microchannel sidewalls. *Analytical chemistry* **2014**, *86* (10), 5083−5088.

(31) Bachman, H.; Chen, C.; Rufo, J.; Zhao, S.; Yang, S.; Tian, Z.; Nama, N.; Huang, P.-H.; Huang, T. J. An acoustofluidic device for efficient mixing over a wide range of flow rates. *Lab Chip* **2020**, *20* (7), 1238−1248.

(32) Rupal, B. S.; Garcia, E. A.; Ayranci, C.; Qureshi, A. J. 3D printed 3d-microfluidics: Recent developments and design challenges. *Journal of Integrated Design and Process Science* 2019, 22 (1), 5−20.

(33) Su, R.; Wang, F.; McAlpine, M. C. 3D printed microfluidics: advances in strategies, integration, and applications. *Lab Chip* 2023, 23 (5), 1279−1299.

(34) Hong, T.-F.; Ju, W.-J.; Wu, M.-C.; Tai, C.-H.; Tsai, C.-H.; Fu, L.-M. Rapid prototyping of PMMA microfluidic chips utilizing a CO 2 laser. *Microfluid. Nanofluid.* 2010, 9, 1125−1133.

(35) Fallahi, H.; Zhang, J.; Phan, H.-P.; Nguyen, N.-T. Flexible microfluidics: Fundamentals, recent developments, and applications. *Micromachines* 2019, 10 (12), 830.

(36) Fallahi, H.; Zhang, J.; Nicholls, J.; Phan, H.-P.; Nguyen, N.-T. Stretchable inertial microfluidic device for tunable particle separation. *Anal. Chem.* 2020, 92 (18), 12473−12480.

(37) Shakeri, A.; Khan, S.; Didar, T. F. Conventional and emerging strategies for the fabrication and functionalization of PDMS-based microfluidic devices. *Lab Chip* 2021, 21 (16), 3053−3075.

(38) Lin, L.; Chung, C.-K. PDMS microfabrication and design for microfluidics and sustainable energy application. *Micromachines* 2021, 12 (11), 1350.

(39) Fallahi, H.; Yadav, S.; Phan, H.-P.; Ta, H.; Zhang, J.; Nguyen, N.-T. Size-tuneable isolation of cancer cells using stretchable inertial microfluidics. *Lab Chip* 2021, 21 (10), 2008−2018.

(40) Akogwu, O.; Kwabi, D.; Midturi, S.; Eleruja, M.; Babatope, B.; Soboyejo, W. O. Large strain deformation and cracking of nano-scale gold films on PDMS substrate. *Mater. Sci. Eng.: B* 2010, 170 (1), 32−40.

(41) Sun, M.; Zhou, X.; Quan, Y.; Zhang, L.; Xie, Y. Highly flexible elastomer microfluidic chip for single cell manipulation. *Biomicrofluidics* 2022, 16 (2), No. 024104.

(42) Jia, Z.; Wu, J.; Wu, X.; Yuan, Q.; Chan, Y.; Liu, B.; Zhang, J.; Yan, S. Size-tunable elasto-inertial sorting of Haematococcus pluvialis in the ultrastretchable microchannel. *Anal. Chem.* 2023, 95 (35), 13338−13345.

(43) Zhang, J.; Yan, S.; Yuan, D.; Alici, G.; Nguyen, N.-T.; Warkiani, M. E.; Li, W. Fundamentals and applications of inertial microfluidics: A review. *Lab Chip* 2016, 16 (1), 10−34.

(44) Zhang, J.; Li, W.; Alici, G. Inertial microfluidics: mechanisms and applications. *Advanced mechatronics and mems devices ii* 2017, 563−593.

(45) Park, J.-S.; Song, S.-H.; Jung, H.-I. Continuous focusing of microparticles using inertial lift force and vorticity via multi-orifice microfluidic channels. *Lab Chip* 2009, 9 (7), 939−948.

(46) Gou, Y.; Jia, Y.; Wang, P.; Sun, C. Progress of inertial microfluidics in principle and application. *Sensors* 2018, 18 (6), 1762.

(47) Kim, G.-Y.; Han, J.-I.; Park, J.-K. Inertial microfluidics-based cell sorting. *BioChip Journal* 2018, 12, 257−267.

(48) Hettiarachchi, S.; Ouyang, L.; Cha, H.; Hansen, H. H.; An, H.; Nguyen, N.-T.; Zhang, J. Viscoelastic microfluidics for enhanced separation resolution of submicron particles and extracellular vesicles. *Nanoscale* 2024, 16 (7), 3560−3570.

(49) Yuan, D.; Zhang, J.; Yan, S.; Pan, C.; Alici, G.; Nguyen, N. T.; Li, W. H. Dean-flow-coupled elasto-inertial three-dimensional particle focusing under viscoelastic flow in a straight channel with asymmetrical expansion−contraction cavity arrays. *Biomicrofluidics* 2015, 9 (4), No. 044108.

(50) Wojcik, B.; LaRuez, J.; Cromer, M.; Villasmil Urdaneta, L. A. The Role of Elasticity in the Vortex Formation in Polymeric Flow around a Sharp Bend. *Applied Sciences* 2021, 11 (14), 6588.

(51) Lu, Y.; Tan, W.; Shi, X.; Liu, M.; Zhu, G. A weak shear stress microfluidic device based on viscoelastic stagnant region (VSR) for biosensitive particle capture. *Talanta* 2021, 233, No. 122550.

(52) Zhou, Y.; Ma, Z.; Ai, Y. Dynamically tunable elasto-inertial particle focusing and sorting in microfluidics. *Lab Chip* 2020, 20 (3), 568−581.

(53) Cha, H.; Fallahi, H.; Dai, Y.; Yuan, D.; An, H.; Nguyen, N.-T.; Zhang, J. Multiphysics microfluidics for cell manipulation and separation: a review. *Lab Chip* 2022, 22 (3), 423−444.

(54) Nguyen, H.-T.; Thach, H.; Roy, E.; Huynh, K.; Perrault, C. M.-T. Low-cost, accessible fabrication methods for microfluidics research in low-resource settings. *Micromachines* 2018, 9 (9), 461.

(55) Kashaninejad, N.; Nguyen, N.-T. Microfluidic solutions for biofluids handling in on-skin wearable systems. *Lab Chip* 2023, 23 (5), 913−937.

(56) Lachaux, J.; Alcaine, C.; Gómez-Escoda, B.; Perrault, C. M.; Duplan, D. O.; Wu, P. Y. J.; Ochoa, I.; Fernandez, L.; Mercier, O.; Coudreuse, D.; Roy, E. Thermoplastic elastomer with advanced hydrophilization and bonding performances for rapid (30 s) and easy molding of microfluidic devices. *Lab Chip* 2017, 17 (15), 2581−2594.

(57) McMillan, A. H.; Thomée, E. K.; Dellaquila, A.; Nassman, H.; Segura, T.; Lesher-Pérez, S. C. Rapid fabrication of membrane-integrated thermoplastic elastomer microfluidic devices. *Micromachines* 2020, 11 (8), 731.

(58) Salmon, H.; Rasouli, M. R.; Distasio, N.; Tabrizian, M. Facile engineering and interfacing of styrenic block copolymers devices for low-cost, multipurpose microfluidic applications. *Eng. Rep.* 2021, 3 (7), No. e12361.

(59) Zhang, J.; Yuan, D.; Zhao, Q.; Teo, A. J. T.; Yan, S.; Ooi, C. H.; Li, W.; Nguyen, N.-T. Fundamentals of Differential Particle Inertial Focusing in Symmetric Sinusoidal Microchannels. *Anal. Chem.* 2019, 91 (6), 4077−4084.

(60) Huang, P.; Feng, J.; Hu, H. H.; Joseph, D. D. Direct simulation of the motion of solid particles in Couette and Poiseuille flows of viscoelastic fluids. *J. Fluid Mech.* 1997, 343, 73−94.

(61) Feng, J.; Huang, P.; Joseph, D. Dynamic simulation of sedimentation of solid particles in an Oldroyd-B fluid. *J. Non-Newtonian Fluid Mech.* 1996, 63 (1), 63−88.

(62) Yuan, D.; Zhao, Q.; Yan, S.; Tang, S.-Y.; Zhang, Y.; Yun, G.; Nguyen, N.-T.; Zhang, J.; Li, M.; Li, W. Sheathless separation of microalgae from bacteria using a simple straight channel based on viscoelastic microfluidics. *Lab Chip* 2019, 19 (17), 2811−2821.